Contents lists available at ScienceDirect

Biomaterials

journal homepage: www.elsevier.com/locate/biomaterials

The morphology of anisotropic 3D-printed hydroxyapatite scaffolds

Fabienne C. Fierz [a,b], Felix Beckmann [c], Marius Huser [b], Stephan H. Irsen [d], Barbara Leukers [d], Frank Witte [e], Özer Degistirici [f], Adrian Andronache [b], Michael Thie [f], Bert Müller [a,b,g,*]

[a] Biomaterials Science Center, University of Basel, 4031 Basel, Switzerland
[b] Computer Vision Laboratory, ETH Zürich, 8092 Zürich, Switzerland
[c] Institute of Materials Research, GKSS Research Center, 21502 Geesthacht, Germany
[d] Caesar Research Center, 53175 Bonn, Germany
[e] Laboratory for Biomechanics and Biomaterials, Department of Orthopaedic Surgery, Hannover Medical School, 30625 Hannover, Germany
[f] Dental Cell Biology, Caesar Research Center, 53175 Bonn, Germany
[g] Materials Science Institute, Dental School, University of Basel, 4056 Basel, Switzerland

ARTICLE INFO

ABSTRACT

Three-dimensional (3D) scaffolds with tailored pores ranging from the nanometer to millimeter scale can support the reconstruction of centimeter-sized osseous defects. Three-dimensional-printing processes permit the voxel-wise fabrication of scaffolds. The present study rests upon 3D-printing with nano-porous hydroxyapatite granulates. The cylindrical design refers to a hollow bone with higher density at the periphery. The millimeter-wide central channel follows the symmetry axis and connects the perpendicularly arranged micro-pores. Synchrotron radiation-based micro computed tomography has served for the non-destructive characterization of the scaffolds. The 3D data treatment is essential, since, for example, the two-dimensional distance maps overestimate the mean distances to the material by 33–50% with respect to the 3D analysis. The scaffolds contain 70% micrometer-wide pores that are interconnected. Using virtual spheres, which might be related to the cells migrating along the pores, the central channel remains accessible through the micro-pores for spheres with a diameter of up to (350 ± 35) μm. Registering the tomograms with their 3D-printing matrices has yielded the almost isotropic shrinking of (27 ± 2)% owing to the sintering process. This registration also allows comparing the design and tomographic data in a quantitative manner to extract the quality of the fabricated scaffolds. Histological analysis of the scaffolds seeded with osteogenic-stimulated progenitor cells has confirmed the suitability of the 3D-printed scaffolds for potential clinical applications.

© 2008 Elsevier Ltd. All rights reserved.

1. Introduction

Over one million operations per annum involve bone repair [1]. By means of synthetic substitutes the bone in-growth and the related healing of larger bony defects are accelerated. Culturing autogenous osteogenic cells on these porous synthetic substitutes to fill larger bone defects belongs to the promising alternatives to the prevailing use of auto-, allo- or xenografts. The synthetic scaffolds for bone augmentation should not only fill the cavity, but also serve as a 3D template for initial cell in-growth and subsequent tissue formation. Besides biocompatibility and mechanical stability, porosity with a high degree of interconnection is of key importance. To ensure cell viability and function, scaffolds ideally need to exhibit porosity spanning different length scales: nano-porosity to allow for molecule transport essential for any nutrition, waste removal and signaling; micro-pores to ensure cell migration and capillary formation; and millimeter-wide pores to incorporate nerves and blood vessels. Vascularization accompanies the intended bone formation [2].

In designing the scaffold's architecture, a balance between the high degree of porosity and reasonable mechanical stability needs to be accomplished. Following the natural architecture of hollow bones, the scaffold should have a cylindrical shape with a rather compact periphery to take the load-bearing function similar to the compacta, while the interior could be porous like the spongiosa. As described by Leong [3], scaffolds need to possess open and interconnected pores that allow cell in-growth and provide the necessary space for neo-vascularization. The required pore diameters, however, are still under discussion. The published values for the optimal mean pore diameters range from 200 to 500 μm [4–6]. The pore lengths are also crucial, because problems of insufficient bone in-growth into the center of the scaffold are encountered and described [7,8].

* Corresponding author. Biomaterials Science Center (BMC), University of Basel, c/o University Hospital Basel, CH-4031 Basel, Switzerland. Tel.: +41 61 265 9660; fax: +41 61 265 9699.
E-mail address: bert.mueller@unibas.ch (B. Müller).

Hydroxyapatite (HA), as the principal mineral component of bone, is well accepted to be osteoconductive [9] and, therefore, qualified for scaffolds in bone tissue engineering [6]. Spray-dried HA granulates can guarantee adequate nano-porosity and serve for 3D-printed scaffolds [10] to manufacture patient-specific implants [11] with pre-defined architecture [3,12]. The precise morphological characterization of the HA scaffolds, however, is missing. Hence, the quality of the fabricated constructs cannot be determined and subsequently optimized in a constitutive fashion. First, an appropriate method to uncover the 3D morphology down to about 1 μm has to be applied, that is synchrotron radiation-based micro computed tomography (SRμCT), which provides the necessary spatial and density resolution. Second, sophisticated computer codes for the 3D evaluation of the GB-data sets must be adapted and further generated. In order to gain dedicated feedback for improving the design and fabrication processes of scaffolds, sensitive parameters for 3D porosity analysis have to be described. It needs to be verified that the simpler and better established 2D tools do not give rise to satisfactory estimates. Although the quantitative characterization of the scaffold's morphology is inherently fundamental, the efficacy of the porous HA scaffolds has to be proven by cell experiments before any animal or clinical study can be initiated.

2. Materials and methods

2.1. Scaffold fabrication

Three hydroxyapatite (HA) scaffolds labeled A, B and C were designed pixel- and layer-wise. The scaffolds were fabricated using an experimental 3D-printing setup described in Ref. [10]. Cubic voxels with the edge length of 240 μm were chosen, which corresponds to the printer resolution of 106 dpi and a layer thickness of 240 μm. The scaffolds with a total height of 30 voxels were constructed out of 15 alternating double-layers corresponding to the two differently designed, circularly shaped printing matrices shown in Fig. 1. A millimeter-wide central channel with a minimal width of 4 voxel lengths (4×240 μm) runs axially through the scaffold. It is connected to a micro-channel network, which opens to the periphery by 8 (Design A) or 12 (Designs B and C) pores per double-layer. In order to define the azimuthal orientation, one additional block of 3 by 3 voxels was attached to the fourth double-

layer on the scaffold's surface (see Fig. 1, shown in the third row). The cylindrical design ensures that for the SRμCT measurements the total X-ray absorption is comparable in all directions of the horizontal plane.

As building materials, spray-dried hydroxyapatite (HA) granules with a mean diameter of 22 μm [13] and a water-based polymer binder solution were used. The polymer binder was removed at the temperature of 450 °C. To obtain scaffolds consisting of pure HA [14] of a sufficiently high mechanical stability, the scaffolds were sintered in air (Chamber Furnace RHF 17/10E; Carbolite GmbH, Ubstadt-Weiher, Germany) at the temperature of 1250 °C for 2 h.

2.2. Cell biology

The 3D HA scaffolds were seeded with human multi-potent dental neural crest-derived progenitor cells (dNC-PCs), which were cultured as previously described [15]. Written consent was obtained from all parents of the participating patients before tooth extraction according to the local regulations and the ethical guidelines. Briefly, the apical pads of the immature tooth were surgically removed, mechanically dissociated and digested with collagenase/dispase (Sigma, Deisenhofen, Germany) at the temperature of 37 °C for 1 h. Subsequently, the harvested tissues including dNC-PCs were plated in the growth medium, low glucose Dulbecco's Modified Eagle Medium (Cambrex Bio Science, Verviers, Belgium) containing 10% fetal calf serum (Biochrom, Berlin, Germany), in a 5% CO_2-atmosphere at the temperature of 37 °C. The cells from passage four were trypsinized, and each scaffold was statically loaded from the top with 2×10^5 cells in 80 μl medium. The cells-scaffold constructs were incubated in the 5% CO_2-atmosphere at the temperature of 37 °C for 2 h. The cells were further cultured in the osteogenic medium, namely the growth medium supplemented with 50 μM ascorbic acid-2-phosphate (Sigma), 100 nM dexamethasone (Sigma), 1 mM ß-glycerol-phosphate (Sigma).

After 28 days the cell-scaffold constructs were fixed in 4% paraformaldehyde for 24 h. They were stored in 0.5 ml Eppendorf tubes filled with phosphate buffered saline (PBS) for the SRμCT measurements. Histological analysis was performed on the HA scaffolds seeded with dNC-PCs. After decalcification with 10% ethylenediaminetetraacetic acid (VWR, Darmstadt, Germany) in Tris buffered saline for 7 days, the constructs were embedded into paraffin and subsequently sectioned (HM 355 S; Microm International GmbH, Walldorf, Germany). The 5 μm-thick slices obtained were stained with hematoxylin–eosin (H and E). To obtain non-decalcified sections of the HA scaffolds seeded with dNC-PCs, they were again fixed in 4% paraformaldehyde. After embedding and polymerization in methyl-methacrylate (Technovit 9100 New Heraeus-Kulzer, Hanau, Germany) according to the manufacturer's instructions, 5 μm-thick sections were cut using a RM 2155 microtome (Leica, Bensheim, Germany). Prior to the staining procedure, the sections were first deacrylated in xylol (2×15 min) and 2-methoxyethylacetate (2×10 min), cleared through the decreasing ethanol series ($2 \times$ isopropyl alcohol, $2 \times 96\%$ ethanol, $2 \times 70\%$ ethanol, 2 min each), and re-hydrated with distilled water. As general staining, the re-hydrated sections were incubated in 0.1% toluidine blue O (Sigma, Seelze, Germany) for 20 s, washed in distilled water, dehydrated in ethanol, and mounted in Eukitt (Labonord, Mönchengladbach, Germany). Photomicrographs were taken with a Zeiss Axioskop 40 or a Zeiss Imager Z1 microscope equipped with a scanning stage, both combined with a Zeiss AxioCam MRc digital camera and Zeiss AxioVision software (Oberkochen, Germany).

2.3. Imaging

SRμCT measurements were performed to quantitatively characterize the blank HA scaffolds and the cell seeded scaffolds in the Eppendorf tubes. The measurements were carried out at the beamline W 2 operated by GKSS Research Center at HASYLAB at DESY, Hamburg, Germany in the absorption contrast mode using photon energy of 30 keV [16]. The pixel length of the acquired projections corresponds to 3.7 μm. The spatial resolution of the entire setup was determined to be 6.0 μm by the modulation transfer function [17]. The 3D data were obtained by means of the standard filtered back-projection reconstruction algorithm out of 721 projections [18]. For easier handling, the data were reduced by binning with a factor of 3 after the reconstruction that results in better density resolution with a pixel length of 11.1 μm [19]. As the scaffolds were larger than the field of view, they were scanned at different height levels. Therefore, it was necessary to register and combine the 3D data to obtain one tomogram for each scaffold. To keep this procedure simple, the registration was done after the reconstruction with voxel resolution.

Complementary to the tomographic imaging, SEM experiments were carried out with an acceleration voltage of 5 kV (Supra 55 SEM; Carl Zeiss AG, Oberkochen, Germany) to show the morphology of the individual granules forming the scaffold with higher magnification, i.e. further down to the nanometer scale. After fixation with glutaraldehyde, the samples were dried in air and coated with about 5 nm-thick gold films using a sputtering machine (MED 020; Bal-Tec, Balzers, Liechtenstein).

2.4. Data analysis

The software VGStudio MAX 1.2 (Volume Graphics, Heidelberg, Germany) served for the visualization of the tomographic data.
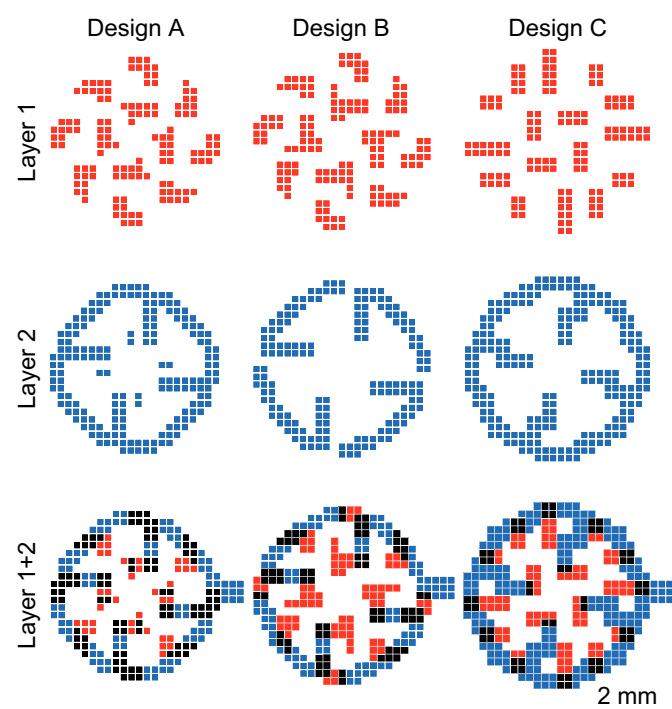

Fig. 1. The input data for the 3D printer (printing matrices) consist of alternating layers shown in red and blue. The overlay of the layers in the third row demonstrates the formation of the stabilizing struts represented in black.

To determine the scaffolds' shrinking as a result of the sinter process, the affine registration algorithm with nine independent parameters (three translational, three rotational, three scaling degrees of freedom) [20] was applied to the acquired tomograms and the corresponding 3D-printing matrices. This affine registration acts on data sets with similar voxel sizes. Therefore, the printing matrices were re-sampled to 240 $\mu m/21 \cong 14$ μm-wide voxels. The starting parameters for the registration were estimated manually. After registration, the top and the bottom regions of the scaffolds were removed in a uniform manner for the three designs to get rid of artifacts at the scaffold borders.

To obtain the binary data set, a threshold for segmenting the HA material from air in the tomograms was chosen based on the histogram of absorption coefficients derived from the SRμCT measurements. The histogram exhibited two distinct peaks relating to air and to the HA material. A further peak overlapping the air peak arose from the glue used for fixation, which partially penetrated into the scaffold. The threshold was set to the mean value of the air and HA peak positions, a reasonable choice as recently demonstrated [21].

The experimentally limited photon statistics always lead to noise and related artifacts resulting in small, virtual particles not connected to the scaffold and small virtual pores within the HA material, respectively. To eliminate these artifacts, particles and pores smaller than 20 voxels were labeled using the software module IL-PoreCal CC (Image Lab GmbH, Winterthur, Switzerland). The total volume of particles smaller than 20 voxels constituted merely 1.2% of the total volume of pores smaller than 20 voxels within HA. This implies that a significant amount of these small pores is indeed present and does not arise from noise. Thus, only the non-connected particles were removed using the software module IL-PoreCal CC while the small pores were not corrected for the noise artifacts.

Further dedicated software packages were developed for the quantitative analysis of data in collaboration with Image Lab GmbH, Winterthur, Switzerland using the open-sourced script language Tcl/Tk [22], IDL 6.4 (ITT Visual Information Solutions, Boulder, CO, USA) and the VIGRA Computer Vision Library [23].

3. Results and discussion

3.1. Visualization of the pores

Contrary to optical methods, which are limited to visualizing the outer shape of the opaque scaffolds (see Fig. 2), the tomographic data allow representing any desired virtual cut through the scaffold. The vertical cut shown in Fig. 2 offers a view onto the interconnected pores and in particular onto the central channel. The dynamic range of the absorption values permits discrimination between HA of different densities, but does not allow segmenting the cells from their extra-cellular matrix or the surrounding PBS.

The spatial resolution of SRμCT is restricted to a few micrometers. Therefore, SEM was applied to characterize the scaffold surface with nanometer resolution to uncover the individual sintered granules with their central opening consisting of HA grains (see Fig. 3a and b). Indeed, Fig. 3b clearly shows the grain boundaries and the nanometer-sized orifices in-between. Note, that for this investigation an area with low cell density was selected. Here, one can recognize single cells adhered to the granules forming a kind of network between the open hollow spheres.

3.2. Determination of shrinkage

The removal of the polymer binder solution and the sinter processes lead to significant shrinking of the 3D-printed scaffolds. This shrinkage was computed for the three orthogonal directions using the scaling parameters from the registration of the 3D-printing matrices and the related tomograms. The shrinking parameters of $(27 \pm 2)\%$ without significant difference between the three designs correspond to values of other studies [10,24–26]. Despite the cylindrical design, shrinking is found to be isotropic, which can be explained by the usage of spherical granules and the cuboid printing dots. The green-body granules contained 30% organic additives that are removed at temperatures of 450 °C. Preliminary data show that this process leads to the shrinkage of only around 1%. Therefore, we can conclude that the densification of the HA grains within the granules mainly causes shrinkage. To realize relatively high degrees of porosity, the densification is only thermally driven without the application of any external force (except gravity). It should be mentioned that the granules did not collapse during sintering and form only small contact areas in-between,
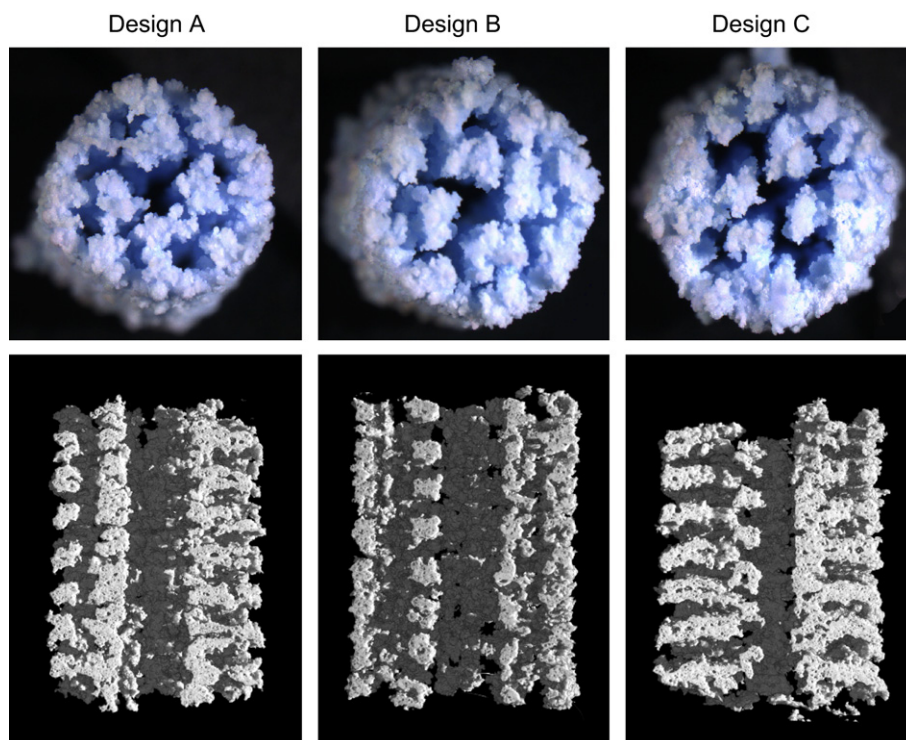

Fig. 2. The photographs in the first row provide a top view of the opaque 3D-printed HA scaffolds with the central channel. The tomographic data can be used to produce any desired virtual cut of the different scaffolds, for example visualizing the internal morphology by the axial cut presented in the second row. The diameters of the scaffolds range from 3.9 to 4.2 mm and the minimal diameters of the central channel from 0.70 to 0.87 mm for Designs A, B and C, respectively.
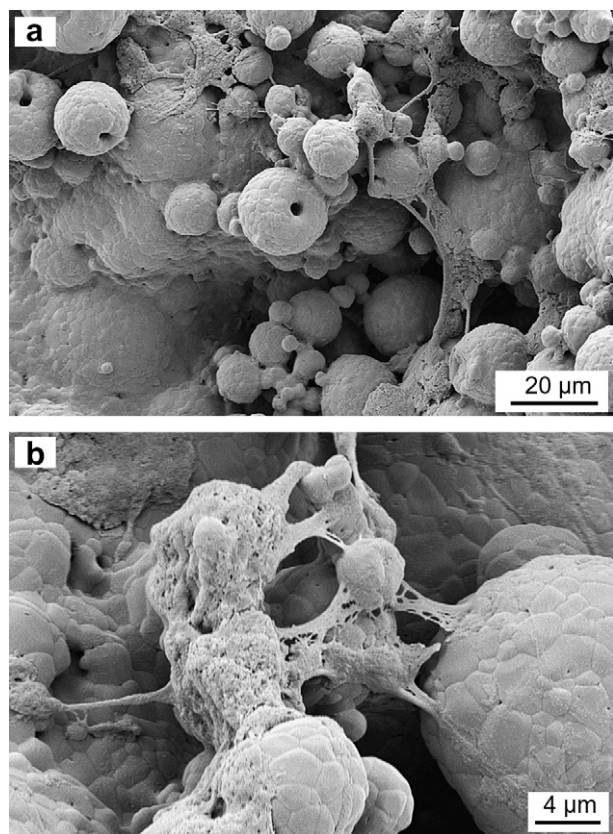
Fig. 3. SEM images of the scaffold's surface with some cells show (a) several granules with the central opening and (b) the nanometer-sized orifices at the grain boundaries.

resulting in relatively high degrees of porosity but rather poor mechanical properties. Contrary to the mechanical properties, the isotropic shrinkage of the 3D-printed HA scaffolds does not depend on the design, which facilitates the fabrication of patient-specific implants.

3.3. Quality assessment of the scaffolds

Using the affine registration one can not only precisely measure the shrinkage, but also quantify how well the fabricated scaffolds match their printing matrices. The HA-related voxels, which lay either inside or outside the matrices in the registered data sets, were determined separately for Layer 1 and Layer 2. Fig. 4 shows the matrices registered with the tomograms elucidating the extent of congruence. Table 1 lists the relative HA volume located outside the registered matrices and the relative volume of HA vacancies detected inside the registered matrices for the different designs and layers. From these data, the print quality follows that amounts to $(30.0 \pm 7.7)\%$. For Layer 2 in the three designs, the volume of HA printed outside the matrices is significantly smaller than the volume of HA vacancies within the matrices. This apparent material loss relates to dot overlapping that concentrates the liquid within smaller volumes. The results given in Table 1 indicate that the print quality of Layer 2 is generally better than that of Layer 1. This can be explained by the larger amount of connected dots forming the ring-like structure. Here, the binder droplets overlap, which improves the wettability of the granules. Furthermore, the bimodal granule size distribution with significant size class difference can result in segregation of the granules. The segregation is expected during the printing process, when the granules are spread to the building platform, and more important for the separated dots during the re-coating when the granules are spread to the building platform [27]. Application of the bimodal granule size
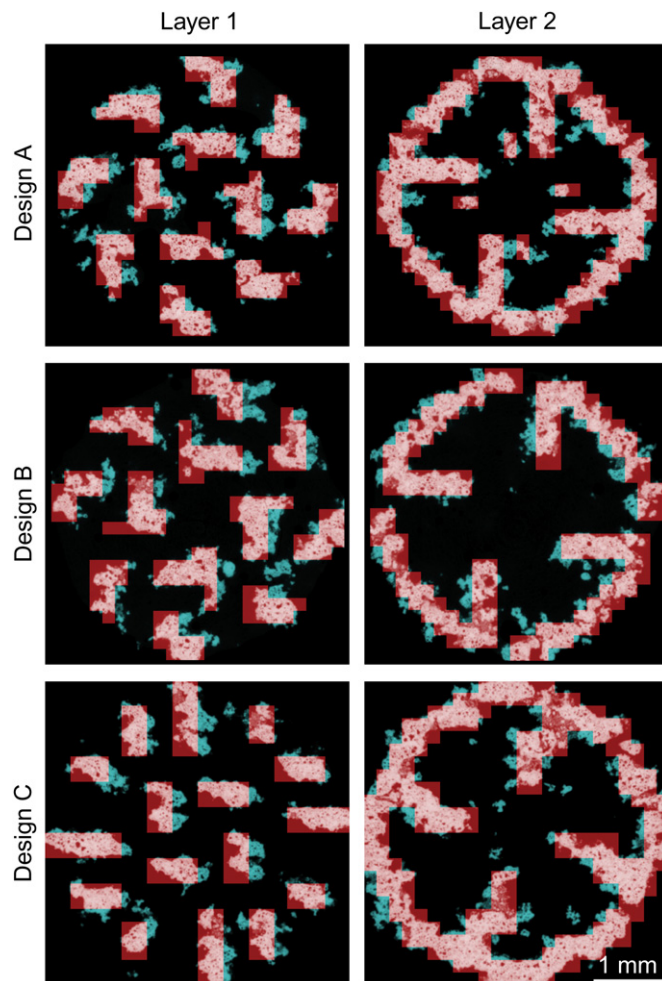

Fig. 4. Two selected slices representing Layers 1 and 2 of each scaffold registered with their printing matrices are shown. The printing matrix consists of the red- and light red-colored areas, the material printed outside the building matrix is shown in turquoise, and the material printed inside the building matrix in light red.

distribution, however, improves the surface quality of the 3D-printed parts [28]. It is important to mention that 100% print quality is not the final aim since the observed rounded HA structures and incorporated niches are beneficial for cell migration compared to sharp edges given by the printing matrices.

3.4. Radial density distribution

For the analysis of the radial density of the HA scaffolds, the software module IL-PoreCal RD (Image Lab GmbH) was developed. This module permits to determine the radial distribution of HA summing up the relative amount of HA voxels from the axis of the

Table 1
To assess the printing quality of the scaffold in a quantitative manner, the volume of HA outside the registered matrices and the volume of HA vacancies within the registered matrices relative to the volume of the related matrices were calculated for Layers 1 and 2 of each design

	HA outside the registered matrix [%][a]	Vacancies within the registered matrix [%][a]
Design A Layer 1	33.2 ± 5.2	30.8 ± 3.9
Design A Layer 2	16.2 ± 3.1	30.2 ± 2.3
Design B Layer 1	30.6 ± 3.0	35.5 ± 1.8
Design B Layer 2	25.2 ± 2.0	31.4 ± 1.5
Design C Layer 1	43.1 ± 8.7	36.7 ± 2.3
Design C Layer 2	16.7 ± 2.3	30.7 ± 2.3

[a] Values are given as the mean standard deviation.

central channel to the scaffold's border. The radial density distribution was separately calculated for Layer 1 and Layer 2 for each sintered scaffold and the related printing matrix. The corresponding plots for Layer 2 are represented in Fig. 5 to show reasonable agreement between the tomogram and the registered matrix. Both curves exhibit the main peak that corresponds to the ring-like structure of Layer 2. Between this main peak and the central channel one recognizes the expected radial density variations. The fabricated scaffolds yielded smaller, rounded maxima as given by the matrices. The lower filling levels for the actual scaffolds compared to the printing matrices can be attributed to the nano- and micro-porosity of the HA material. The borders of the scaffolds,

which increase by 88 μm from Design A through C as illustrated by the dashed vertical lines in Fig. 5, reflect their radii. The radii of the central channels relate to radial distances of up to 0.5 mm, where the filling level is close to zero. These values as the integral number along the central axis yield a spatial resolution much better than the pixel size of the 3D printer. The radial density distribution permits a direct comparison of different radially designed scaffolds even with regard to the architecture of the natural hollow bone. Furthermore, the tool may help to determine the depth of bone ingrowth in cylindrically shaped implants similar to applying a radial grid as done by Chu et al. [29].

3.5. Distance mapping

From the medical and biological points of view, the mean pore diameter is a frequently used parameter. For pores with rough surfaces, however, distance mapping is the more suitable approach [30,31]. In order to demonstrate the necessity of 3D data evaluation, we have compared the 2D and 3D distance maps. The software module IL-PoreCal DM (Image Lab GmbH) developed in a previous study [30] determines the minimal distance of each pixel (2D transform) or voxel (3D transform) to the scaffold material. Fig. 6 shows the 2D and 3D distance maps of two selected slices representing Layer 1 and 2 of Design A. As illustrated by the different colors, the distances are significantly larger for the 2D analysis. For the calculation of the distance distribution histograms given in Fig. 7, the volume of interest, i.e. the scaffold with its pores, needed to be separated from the surrounding air volume. This was accomplished by applying the outline masks based on the printing
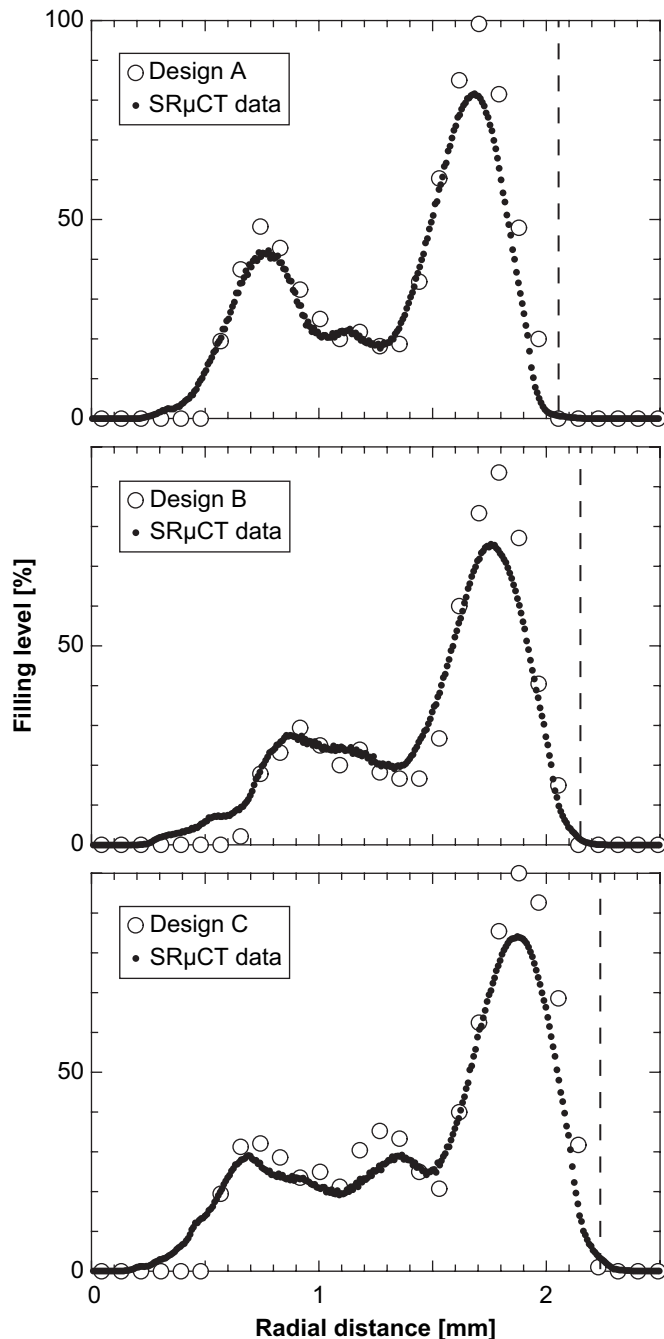

Fig. 5. The radial density distribution corresponds to the fraction of material starting from the sample's center ranging to the circumferential surface. Hence, the filling level is complementary to porosity. The graphs of the radial density distribution of the sintered scaffolds (data A–C, Layer 2) and their printing matrices (Design A–C, Layer 2) show reasonable agreement.
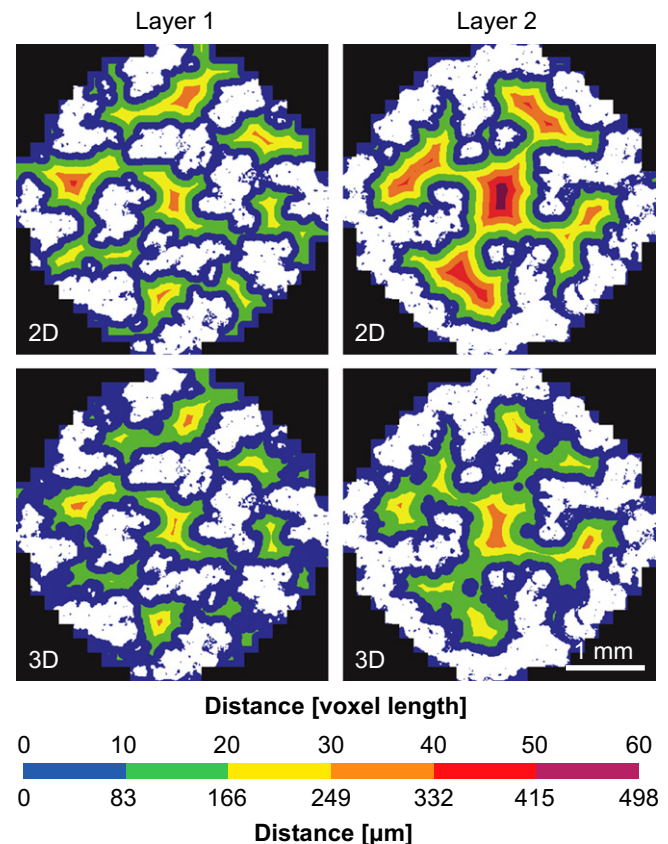

Fig. 6. Comparison of 2D and 3D distance maps of Design A, Layers 1 and 2, shows that the 2D analysis significantly overestimates the pore diameters. The minimal distance of each pixel (2D transform) or voxel (3D transform) to the material is indicated according to the color bar. White corresponds to the HA material and black to the mask, which confines the volume of interest.
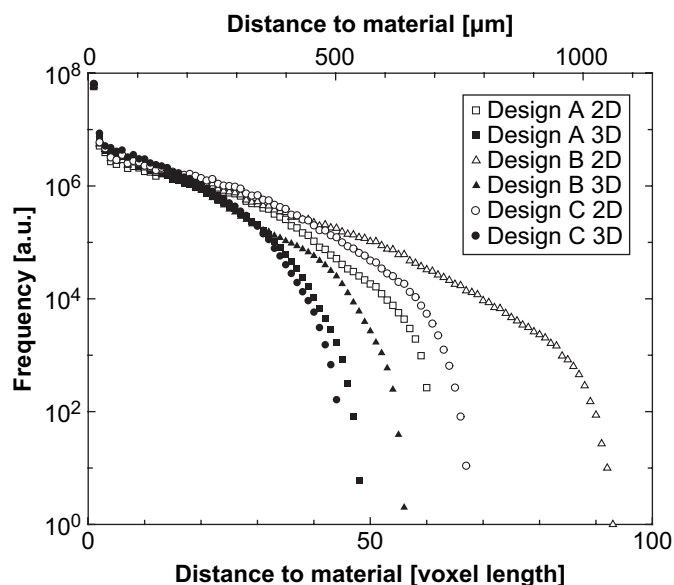
Fig. 7. The histograms of the minimal distances to the material resulting from the 2D and 3D distance transforms demonstrate that the differences between the 2D and 3D analyses depend on the scaffold design.

matrices as visualized for Design A in Fig. 6 by the black areas. The comparison of the mean distances to the material confirmed that the 2D analysis provides values that overestimate the actual ones using the 3D analysis by 33% for Design A, 50% for Design B, and 46% for Design C. The 2D–3D comparison clearly points out the necessity for a 3D analysis. It should be emphasized that the difference between the 2D and 3D analyses is high with respect to our previous study [30] and strongly depends on the scaffold architecture. Since 2D methods overrate the distance to the material by values as high as 50%, conventional optical methods only provide a rough estimate of the mean distance to the material as the upper limit.

3.6. Pore interconnectivity

Since porosity and interconnectivity are important parameters for cell in-growth, the accessibility of the scaffold's porous network to the migrating cells was analyzed using virtual spheres. The accessible pore volumes were calculated for spheres of increasing diameters. The calculation was performed with the binary representation of the six-fold binned 3D data of the scaffold. To avoid access through the central channel from top and bottom and, therefore, to restrict the accessibility of the scaffold via the micropores, additional volume was only added laterally so that the largest spheres considered can be placed onto the lateral surface of the cylindrical scaffold. The smallest sphere is just given by a single voxel. The radius of the virtual sphere is increased voxel-wise in the three orthogonal directions. The balance point of the surrounding voxels determines whether they are considered as part of the spheres of increasing size or not. The same procedure was used to define the 3D distance map. Consequently, it is rather simple to label the pore volume connected to the laterally added part as the function of the sphere radius based on the 3D distance map. Finally, the labeled pore volume has to be dilated by the considered sphere radius.

In order to separate the scaffold from the surrounding air, a sufficiently large sphere with a diameter of 983 μm was used. This choice leads to porosities of 67.2%, 70.3% and 68.4% for Designs A, B and C, respectively. For the smallest sphere diameter of 17 μm the accessible interconnected pore volume cover between 98.7% and 99.2% of the total pore volume in the three designs (see Fig. 8). The
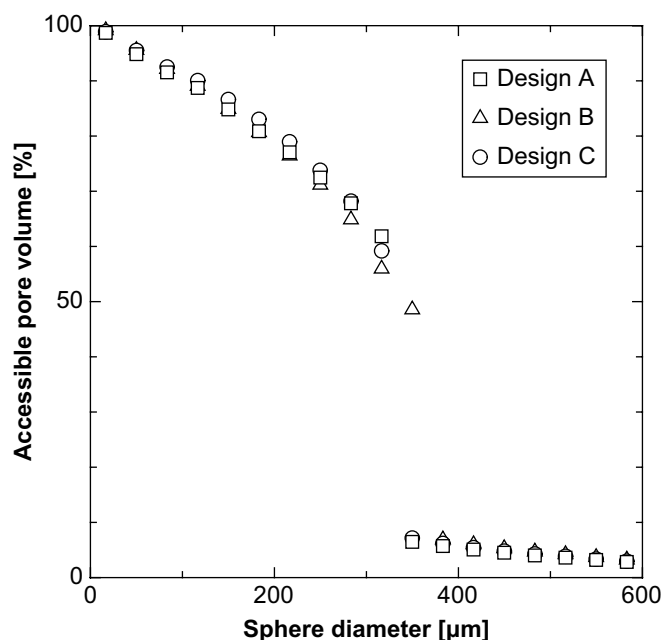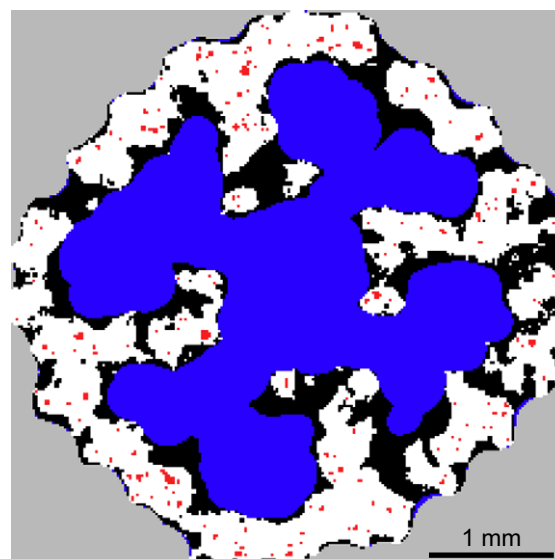

Fig. 8. Percentages of pore volumes accessible to virtual spheres are given as a function of the sphere diameter for Designs A, B and C. In the selected slice of scaffold Design A, the blue-colored area is accessible to the sphere with the diameter of 317 μm, but not for the one with the diameter of 350 μm. The gray-colored region is accessible, whereas the black area is inaccessible to these spheres. Red-colored areas represent pores enclosed in white-colored HA.

accessible volume decreases with the sphere diameter. One observes an abrupt transition from the mainly accessible to inaccessible pore volumes between 300 and 400 μm as illustrated for the selected slice of Design A in Fig. 8. The blue- and gray-colored areas in the tomographic slice are accessible to the sphere with the diameter of 317 μm, whereas only the gray-colored area is accessible to the sphere with the diameter of 350 μm, considering the laterally arranged micro-pores of the scaffold.

3.7. Cell experiments

Fig. 9a shows a selected H and E stained histological slice of the cells-scaffold construct after 28 days of cultivation that mainly contains soft tissues of cells with a fibroblastic morphology and to some extent, especially near the dissolved HA, cells with a cuboidal,
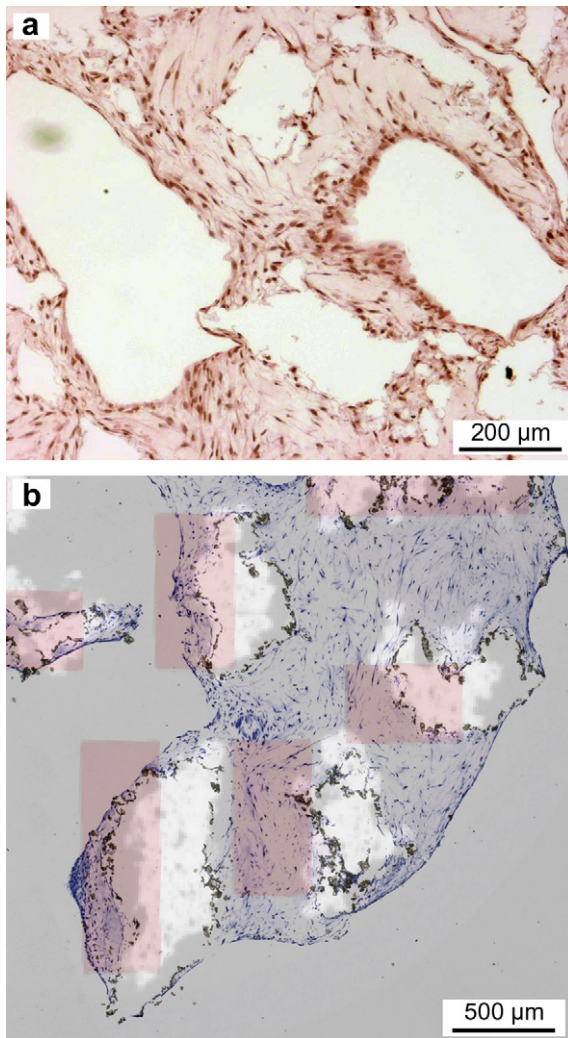
Fig. 9. (a) The image of the decalcified section shows cells of different morphologies. (b) The histological slice of the non-decalcified section (HA scaffold Design C with toluidine blue stained cells) is manually registered with the tomogram (white) and printing matrix (transparent red).

indicates the cytocompatibility of the 3D-printed HA scaffolds. Further series of cell experiments have to be carried out to optimize scaffold fabrication and design for potential clinical applications.

3.8. Scaffold performance

The present study underlines that spray-dried HA is cytocompatible and belongs to the group of promising materials for 3D-printed scaffolds for bone augmentation. The 3D-printed HA scaffolds have pores ranging from molecular to millimeter scales. The nanometer-sized porosity of the hollow HA granules can be altered adapting the relevant parameters of the spray-drying and sintering processes [32]. The sizes and morphologies of the granules determine their packaging implying the presence of small micro-pores. The size of these pores, however, usually does not allow for any cell in-growth, since the cells span across these cavities as shown in Fig. 3.

Three-dimensional-printing enables us to combine patient-specific architectures with the scaffold micro-morphology important for cell behavior and tissue formation. As intended by the scaffold design and verified by the comprehensive analysis, the more than 320 μm-wide micro-pores are interconnected and form an open network connecting the surroundings with the central channel. The central channel is important, since many studies have described insufficient bone in-growth into the center areas of scaffolds [7,8]. Such channels were previously investigated [29,33]. Chu et al. [29] described a radial design, where the 2.5 mm-long micro-channels were perpendicular to the 3 mm-wide central channel. As the cylindrically shaped micro-pores are not interconnected and exhibit a diameter-to-length-ratio of about 1:7, this scaffold design results in a low amount of bone in-growth. The scaffolds of Rose et al. [33] were formed inserting steel needles into the green HA ceramics that led to straight channels. Such an approach, however, limits the shape and the size of the channels. Although the sizes of the micro-pores are comparable to the present study, the average interconnection window of (72 ± 4) μm is significantly smaller than for our 3D-printed scaffolds, which have interconnecting diameters larger than 320 μm.

4. Conclusions

The preparation of scaffolds following biomimetic design rules using rapid prototyping, including 3D-printing with porous HA granules, belongs to key approaches for patient-specific implants to fill larger cavities and to initiate cell in-growth and subsequent tissue formation. The present study demonstrates that the selection of porous HA granules with a suitable morphology for 3D-printing does not only allow fabricating scaffolds with millimeter-sized straight channels but also with rather complex micro-pores about 300 μm in diameter large enough for cell migration. Since the coalesced, sintered HA granules form an interconnected, nano-porous network, processes needed for tissue formation inside the micro-pores such as molecular signaling, nutrition supply, and waste removal become possible, an assumption supported by the presence of a type of connective tissue in the non-decalcified histological sections of the cell seeded scaffolds. It is, however, necessary to optimize the design of the scaffolds on different length scales, in particular on the cellular level. SRμCT, as a non-destructive technique, yields 3D data with the desired micrometer resolution. As elucidated, 3D data evaluation is essential to obtain reliable quantities for scaffold optimization. The large SRμCT data sets together with advanced computer tools for morphological analysis, such as micro-pore analysis, distance mapping, radial density distribution, 3D-registration for the measurement of shrinkage and quality assessment, yield vital feedback to improve the micro-architecture of scaffolds fabricated by any kind of biomaterial to be used in tissue engineering and potential clinical applications.

osteoblast-like morphology. The heterogeneous cell morphologies indicate vital cells developed from the dNC-PCs presumably via distinct differentiation paths.

The determination of the cell location within the scaffold is demanding because the cells are invisible in the SRμCT data and histology requires sectioning without decalcification. The optical micrograph in Fig. 9b is the part of a selected slice of the non-decalcified brittle HA scaffold (Design C) with the toluidine blue stained cells. Such an overview micrograph enables us to determine the location of the cells within the scaffold. For that purpose, the micrograph was manually registered with the tomographic data superimposed in white. Because of the limited print quality, a better impression might be obtained by adding the design (transparent red) that has been automatically 3D-registered to the SRμCT data as described above. The micrograph shows that cells of different morphology fill the micro-pores. Within the 28 days of cultivation the histoid of dNC-PCs differentiated to cells forming a type of connective tissue.

Seeding of the dNC-PCs was inhomogeneous on the entire scaffold preventing the possibility to comprehensively analyze tissue formation as described by Chu et al. [29]. Nevertheless, the presence of a certain type of connective tissue [15], originating from dNC-PCs and exhibiting cells of different morphologies,

Acknowledgements

References

[1] Langer R, Vacanti JP. Tissue engineering. Science 1993;260(5110):920–6.
[2] Weiss P, Obadia L, Magne D, Bourges X, Rau C, Weitkamp T, et al. Synchrotron X-ray microtomography (on a micron scale) provides three-dimensional imaging representation of bone ingrowth in calcium phosphate biomaterials. Biomaterials 2003;24(25):4591–601.
[3] Leong K, Cheah C, Chua C. Solid freeform fabrication of three-dimensional scaffolds for engineering replacement tissues and organs. Biomaterials 2003; 24(13):2363–78.
[4] Boyan BD, Hummert TW, Dean DD, Schwartz Z. Role of material surfaces in regulating bone and cartilage cell response. Biomaterials 1996;17(2):137–46.
[5] Gauthier O, Bouler JM, Aguado E, Pilet P, Daculsi G. Macroporous biphasic calcium phosphate ceramics: influence of macropore diameter and macroporosity percentage on bone ingrowth. Biomaterials 1998;19(1–3):133–9.
[6] Karageorgiou V, Kaplan D. Porosity of 3D biomaterial scaffolds and osteogenesis. Biomaterials 2005;26(27):5474–91.
[7] Otsuki B, Takemoto M, Fujibayashi S, Neo M, Kokubo T, Nakamura T. Pore throat size and connectivity determine bone and tissue ingrowth into porous implants: three-dimensional micro-CT based structural analyses of porous bioactive titanium implants. Biomaterials 2006;27:5892–900.
[8] Ishaug-Riley SL, Crane-Kruger GM, Yaszemski MJ, Mikos AG. Three-dimensional culture of rat calvarial osteoblasts in porous biodegradable polymers. Biomaterials 1998;19(15):1405–12.
[9] LeGeros RZ. Properties of osteoconductive biomaterials: calcium phosphates. Clin Orthop Relat Res 2002;395:81–98.
[10] Seitz H, Rieder W, Irsen S, Leukers B, Tille C. Three-dimensional printing of porous ceramic scaffolds for bone tissue engineering. J Biomed Mater Res B: Appl Biomater 2005;74:782–8.
[11] Schieker M, Seitz H, Drosse I, Seitz S, Mutschler W. Biomaterials as scaffold for bone tissue engineering. Eur J Trauma 2006;32:114–24.
[12] Hutmacher DW. Scaffold design and fabrication technologies for engineering tissues – state of the art and future perspectives. J Biomater Sci Polym Ed 2001;12(1):107–24.
[13] Irsen SH, Leukers B, Hockling C, Tille C, Seitz H. Bioceramic granulates for use in 3D printing: process engineering aspects. Materialwiss Werkst 2006;37: 533–7.
[14] Leukers B, Gulkan H, Irsen S, Milz S, Tille C, Seitz H, et al. Biocompatibility of ceramic scaffolds for bone replacement made by 3D printing. Materialwiss Werkst 2005;36:781–7.
[15] Degistirici O, Jaquiery C, Schoenebeck B, Siemonsmeier J, Goetz W, Martin I, et al. Defining properties of neural crest-derived progenitor cells from the apex of human developing tooth. Tissue Eng: Part A 2008;14(2):317–30.
[16] Beckmann F, Donath T, Fischer J, Dose T, Lippmann T, Lottermoser R, et al. New developments for synchrotron-radiation-based microtomography at DESY. 2006. In: Bonse U, editor. Developments in X-ray tomography V. San Diego: SPIE; 2006. 6318210.
[17] Müller B, Thurner P, Beckmann F, Weitkamp T, Rau C, Bernhardt R, et al. Non-destructive three-dimensional evaluation of biocompatible materials by microtomography using synchrotron radiation. In: Bonse U, editor. Developments in X-ray tomography III. San Diego: SPIE; 2002. p. 178–88.
[18] Kak AC, Slaney M. Principles of computerized tomographic imaging. Philadelphia: SIAM; 2001.
[19] Thurner P, Beckmann F, Müller B. An optimization procedure for spatial and density resolution in hard X-ray micro-computed tomography. Nucl Instrum Methods Phys Res B 2004;225(4):599–603.
[20] Hajnal JV, Hill DLG, Hawkes DJ. Medical image registration. Boca Raton, FL: CRC Press Inc; 2001.
[21] Irsen SH, Leukers B, Bruckschen B, Tille C, Seitz H, Beckmann F, et al. Image-based analysis of the internal microstructure of bone replacement scaffolds fabricated by 3D printing. 2006. In: Bonse U, editor. Developments in X-ray tomography V. San Diego: SPIE; 2006. 631809.
[22] <http://www.tcl.tk/>.
[23] Koethe U. In: Jähne B, Haussecker H, Geissler P, editors. Handbook of computer vision and applications. San Diego: Academic Press; 1999. p. 103–32.
[24] Wilson CE, de Bruijn JD, van Blitterswijk CA, Verbout AJ, Dhert WJA. Design and fabrication of standardized hydroxyapatite scaffolds with a defined macro-architecture by rapid prototyping for bone-tissue-engineering research. J Biomed Mater Res 2004;68A(1):123–32.
[25] Jongpaiboonkit L, Halloran JW, Hollister SJ. Internal structure evaluation of three-dimensional calcium. J Am Ceram Soc 2006;89(10):3176–81.
[26] Yang HY, Yang SF, Chi XP, Evans JRG, Thompson I, Cook RJ, et al. Sintering behaviour of calcium phosphate filaments for use as hard tissue scaffolds. J Eur Ceram Soc 2008;28:159–67.
[27] Lee S-JJ, Sachs E, Cima M. Layer position accuracy in powder-based rapid prototyping. Rapid Prototyping J 1995;1(4):24–37.
[28] Lanzetta M, Sachs E. Improved surface finish in 3D printing using bimodal powder distribution. Rapid Prototyping J 2003;9(3):157–66.
[29] Chu TMG, Orton DG, Hollister SJ, Feinberg SE, Halloran JW. Mechanical and in vivo performance of hydroxyapatite implants with controlled architectures. Biomaterials 2002;23(5):1283–93.
[30] Müller B, Beckmann F, Huser M, Maspero F, Szekely G, Ruffieux K, et al. Non-destructive three-dimensional evaluation of a polymer sponge by micro-tomography using synchrotron radiation. Biomol Eng 2002;19:73–8.
[31] Komlev VS, Peyrin F, Mastrogiacomo M, Cedola A, Papadimitropoulos A, Rustichelli F, et al. Kinetics of in vivo bone deposition by bone marrow stromal cells into porous calcium phosphate scaffolds: an X-ray computed microtomography study. Tissue Eng 2006;12(12):3449–58.
[32] Wang AJ, Lu YP, Sun RX. Recent progress on the fabrication of hollow microspheres. Mater Sci Eng A 2007;460–461:1–6.
[33] Rose FR, Cyster LA, Grant DM, Scotchford CA, Howdle SM, Shakesheff KM. In vitro assessment of cell penetration into porous hydroxyapatite scaffolds with a central aligned channel. Biomaterials 2004;25(24):5507–14.